ROYAL SOCIETY
OF CHEMISTRY

PAPER

Evaluation of $La_{0.3}Sr_{0.7}Ti_{1-x}Co_xO_3$ as a potential cathode material for solid oxide fuel cells

Zhihong Du,[a] Hailei Zhao,*[ac] Yongna Shen,[a] Lu Wang,[a] Mengya Fang,[a] Konrad Świerczek[b] and Kun Zheng[b]

Perovskites $La_{0.3}Sr_{0.7}Ti_{1-x}Co_xO_3$ (LSTCs, $x = 0.3$–0.6) are systematically evaluated as potential cathode materials for solid oxide fuel cells. The effects of Co substitution for Ti on structural characteristics, thermal expansion coefficients (TECs), electrical conductivity, and electrochemical performance are investigated. All of the synthesized LSTCs exhibit a cubic structure. With Rietveld refinement on the high-temperature X-ray diffraction data, the TECs of LSTCs are calculated to be 20–26×10^{-6} K^{-1}. LSTC shows good thermal cycling stability and is chemically compatible with the LSGM electrolyte below 1250 °C. The substitution of Co for Ti increases significantly the electrical conductivity of LSTC. The role of doping on the conduction behavior is discussed based on defect chemistry theory and first principles calculation. The electrochemical performances of LSTC are remarkably improved with Co substitution. The area specific resistance of sample $La_{0.3}Sr_{0.7}Ti_{0.4}Co_{0.6}O_3$ on the $La_{0.8}Sr_{0.2}Ga_{0.8}Mg_{0.2}O_{3-\delta}$ (LSGM) electrolyte in symmetrical cells is 0.0145, 0.0233, 0.0409, 0.0930 Ω cm^2 at 850, 800, 750 and 700 °C, respectively, and the maximum power density of the LSGM electrolyte (400 μm)-supported single cell with the Ni–GDC anode, LDC buffer layer and LSTC cathode reaches 464.5, 648, and 775 mW cm^{-2} at 850 °C for $x = 0.3$, 0.45, and 0.6, respectively. All these results suggest that LSTC are promising candidate cathode materials for SOFCs.

1. Introduction

As electrochemical devices that directly convert the chemical energy of fuels into electricity, solid oxide fuel cells (SOFCs) have attracted lots of attention due to their high efficiency, low emission, noise-free nature and fuel flexibility.[1,2] The SOFC usually works in the temperature range of 900–1000 °C. Lowering the operating temperature can reduce the cost and promote the commercialization of SOFCs.[3–5] Much effort has been made to develop intermediate-temperature SOFCs (IT-SOFCs).[6] However, in the conventional case of the YSZ electrolyte and $La_{1-x}Sr_xMnO_3$ cathode, decreasing the operating temperature leads to a significant increase in both ohmic resistance mainly coming from the electrolyte and polarization resistance primarily from the cathode. For the ohmic resistance, this problem has been gradually solved by reducing the thickness of the electrolyte or employing alternative electrolyte materials like $Gd_{0.1}Ce_{0.9}O_{2-\delta}$ (GDC) and $La(Sr)Ga(Mg)O_3$ (LSGM).[7,8] To address the cathodic polarization, the development of high-performance cathode materials has become

critical. Mixed ionic–electronic conductors (MIEC) like doped $LaCoO_{3-\delta}$,[9–11] La_2NiO_4 (ref. 12–14) and $Ba_{0.5}Sr_{0.5}Co_{0.8}Fe_{0.2}O_{3-\delta}$ (BSCF)[15] have been extensively studied as potential cathode materials considering their high catalytic activity for oxygen reduction at lower and intermediate temperatures.

The cobalt-based perovskites have attracted increasing attention as alternative cathode materials for IT-SOFCs due to their mixed-conducting characteristics and high electrocatalytic activity towards oxygen reduction.[15–17] However, their practical application in IT-SOFCs is severely limited because of their large thermal expansion coefficient (TEC). The previous study reveals that introducing a stable Ti^{4+} ion to replace part of Co ions of $Ba_{0.6}Sr_{0.4}CoO_{3-\delta}$ can successfully decrease the TEC.[18] Recently, $La_{0.5}Sr_{0.5}Co_{0.5}Ti_{0.5}O_3$ is reported to be a good candidate as a symmetrical electrode in IT-SOFCs. It shows good catalytic activity towards oxygen reduction in the cathode side and hydrogen oxidation in the anode side, and keeps good structural stability in both oxidizing and reducing atmospheres.[19]

La-doped $SrTiO_3$ has been reported as a potential anode material for SOFCs due to its high electronic conductivity in reducing atmospheres and good chemical and structural stability upon redox cycling.[20–23] Substituting Ti with Co for $La_{0.3}Sr_{0.7}TiO_3$ (LST) could improve the oxygen ionic conductivity.[24] Taking into account that Co ions usually possess high redox ability, more Co substitution for Ti has the potential to enhance the catalytic activity of LST towards oxygen reduction,

School of Materials Science and Engineering, University of Science and Technology Beijing, Beijing 100083, China. E-mail: hlzhao@ustb.edu.cn; Fax: +86 10 82376837; Tel: +86 10 82376837

AGH University of Science and Technology, Faculty of Energy and Fuels, Department of Hydrogen Energy, al. A. Mickiewicza 30, 30-059 Krakow, Poland

Beijing Key Lab of New Energy Material and Technology, Beijing 100083, China

and thus can turn LST into a cathode material. The stable oxidation state of Ti ions in air ensures good structural stability and a lower TEC value for LST. As symmetrical electrode materials, $La_{0.5}Sr_{0.5}Co_{0.5}Ti_{0.5}O_3$,[19] $La_{0.4}Sr_{0.6}Ti_{1-y}Co_yO_{3-\delta}$ (ref. 25) and $La_{2-x}Sr_xCoTiO_6$,[26] have been investigated recently. These studies focus mainly on the lattice structure evolution of $(LaSr)(TiCo)O_3$ with chemical composition and environmental atmosphere, but less on the electrochemical performance, except for the work on $La_{0.5}Sr_{0.5}Co_{0.5}Ti_{0.5}O_3$.

As B-site elements, the different electronic structures of Ti and Co ions endow perovskite oxides with much different properties, in terms of structural stability, lattice defect, electronic conductivity, and catalytic activity. The Co/Ti ratio will have a strong impact on the electrode performance of $(LaSr)(TiCo)O_3$ materials. In this work, $La_{0.3}Sr_{0.7}Ti_{1-x}Co_xO_3$ (LSTC, $x = 0.3–0.6$) materials are prepared and characterized as cathode materials, with the aim to get a deep understanding of the effect of Co content on the crystal structure, electrical conductivity and electrochemical properties. First principles calculation is employed to elucidate the electronic conduction behavior of LSTC.

2.   Experimental

2.1.   Sample preparation

$La_{0.3}Sr_{0.7}Ti_{1-x}Co_xO_3$ ($x = 0.3–0.6$, LSTC) powders were synthesized by a citric acid–nitrate combustion process, with $Sr(NO_3)_2$ (99.9%, Sinopharm), La_2O_3 (99.9%, Sinopharm), $Co(NH_3)_2 \cdot 6H_2O$ (99.9%, Sinopharm), and $C_{16}H_{36}O_4Ti$ (tetra-n-butyl titanate, 99.9%, Sinopharm) as starting materials and citric acid monohydrate ($C_6H_8O_7 \cdot H_2O$, Guangdong Xilong) as a complexant. Before being used, La_2O_3 was annealed at 1000 °C for 4 h to remove possibly absorbed water and CO_2. First, $C_{16}H_{36}O_4Ti$ was dissolved in ethanol at a molar ratio of 1 : 30 to form a transparent solution, which was then added to a citric acid solution with a pH value of 5 to produce a stable Ti^{4+} aqueous solution, followed by treatment in a water bath at 80 °C for 1 h. The La_2O_3 and nitrate salts were dissolved in dilute nitric acid solution to form metal ion solution, the pH value of which was also adjusted to 5 with ammonia (AR, Sinopharm). Then the two resultant solutions were mixed together thoroughly. The amount of citric acid was fixed at 2 : 1 in molar ratio to the total amount of metal ions.

The obtained final solution was heated in a water bath at 80 °C until a gel was formed. The gel was transferred into an oven and heated at 250 °C to get a fluffy precursor, which was ground and subsequently calcined at 800 °C for 6 h with an interval at 400 °C for 2 h to obtain LSTC powders. The prepared LSTC powders were uniaxially pressed into pellets (19 mm in diameter) and rectangular bars (40 mm × 7 mm × 3 mm) with an appropriate amount of polyvinylalcohol (PVA, 1 wt%) as a binder, followed by sintering at 1200 °C ($x = 0.3, 0.45$) and 1150 °C ($x = 0.6$) for 10 h in air to get dense samples for electrical conductivity measurement.

2.2.   Cell preparation

The $La_{0.8}Sr_{0.2}Ga_{0.8}Mg_{0.2}O_{3-\delta}$ (LSGM), $Gd_{0.1}Ce_{0.9}O_{2-\delta}$ (GDC) and $La_{0.4}Ce_{0.6}O_{2-\delta}$ (LDC) powders were synthesized by the same citric acid–nitrate method.[12] The dense LSGM electrolyte (~400 μm in thickness) was obtained by pressing the calcined powder into disks with a diameter of 19 mm and then sintering at 1450 °C for 8 h. NiO–GDC (6 : 4 in weight ratio) was used as the anode and the prepared LSTC as the cathode. LDC was employed as the buffer layer to prevent the reaction between Ni in the anode and LSGM electrolyte. All the electrolyte-supported cells were fabricated by a screen-printing technique. The electrode slurries were prepared by mixing homogeneously the electrode powders with α-terpineol solution of 6 wt% ethylene cellulose in a weight ratio of 2 : 1. For the LSTC cathode inks, a little amount of flour was used as a pore former.

For symmetrical cells of LSTC|LSGM|LSTC, LSTC slurries were screen-printed on both sides of the LSGM electrolyte symmetrically (active area 0.5 cm^2), followed by calcining at 1200 °C for 2 h. For a single cell with the configuration of Ni–GDC|LDC|LSGM|LSTC, the LDC slurry was deposited on one side of the LSGM electrolyte (active area 0.78 cm^2) and fired at 1400 °C for 2 h. Subsequently, the Ni–GDC anode slurry was screen-printed on the LDC layer and fired at 1300 °C for 2 h. Finally LSTC ($x = 0.3–0.6$) was applied on the other side of the LSGM electrolyte and calcined at 1200 °C for 2 h. The active area of both anode and cathode was 0.5 cm^2. Ag paste was used as the current collector, which was painted in a grid structure on both sides of the cells and fired at 650 °C for 0.5 h. The final cells were sealed on an alumina tube with a ceramic-based sealant (Cerama-bond 552-VFG, Aremco). Humidified H_2 (~3% H_2O) was fed as fuel to the anode with a flow rate of 40 ml min^{-1}, and pure O_2 or air (100 ml min^{-1}) as an oxidant to the cathode.

2.3.   Structural characterization

The phases and crystal structure of LSTC ($x = 0.3–0.6$) samples were identified by X-ray diffraction (XRD, Rigaku D/max-AX-ray diffractometer) with Cu-Kα radiation ($\lambda = 1.5406$ Å). High Temperature XRD (HT-XRD) measurements were carried out on a PANalytical X'Pert Pro diffractometer (operating at 45 kV and 40 mA, with CuKα radiation) with an Anton Paar HTK 1200N oven-chamber over a 2θ range of 10–110° with a step size of 0.013° from room temperature to 900 °C in air. The Rietveld refinements of the XRD patterns were performed using GSAS/EXPGUI software.[27,28] The thermal expansion coefficient of LSTC was calculated with HT-XRD data. Thermogravimetric (TG) measurement was performed on a NETZSCH STA 449F3 between 50 and 835 °C in air with a heating rate of 10 °C min^{-1}. To examine the chemical compatibility of the LSTC cathode with the LSGM electrolyte, the LSTC ($x = 0.6$) powder was mixed uniformly with the LSGM powder in 1 : 1 mass ratio, and then pressed and calcined at 1250 °C for 5 h in air. The calcined pellets were crushed and examined by XRD. X-ray photoelectron spectroscopy (XPS) was used to identify the oxidation state of Co ions in the synthesized LSTC ($x = 0.45$ and 0.6) on a RBD upgraded PHI-5000C ESCA system (Perkin Elmer) with Mg Kα radiation ($h\nu = 1253.6$ eV). The data analysis was carried out by using XPSPeak4.1 provided by Raymund W. M. Kwok (The Chinese University of Hongkong, China). A scanning electron

microscope (SEM, LEO-1450) was employed to observe the microstructure of the sintered dense pellets and cell electrodes.

2.4. First principles calculation

To get insight into the effect of Co-doping on the electronic structure of the LSTC samples, first-principles calculation was performed to get the density of states (DOS) of the material based on density functional theory using Materials Studio (MS) software. The detailed parameter setting was described elsewhere.[29] The structure model of the LSTC material was based on a cubic cell with 40 atoms ($La_2Sr_6Ti_8O_{24}$ and $La_2Sr_6Ti_4Co_4O_{24}$) that corresponded to a $2 \times 2 \times 2$ super cell of the ideal cubic simple ABO_3 perovskite ($Pm\bar{3}m$). $La_2Sr_6Ti_8O_{24}$ and $La_2Sr_6Ti_4Co_4O_{24}$ were used to approximately represent $La_{0.3}Sr_{0.7}TiO_3$ and Co-doped $La_{0.3}Sr_{0.7}Ti_{0.5}Co_{0.5}O_3$, respectively.

2.5. Electrical and electrochemical characterization

The total electrical conductivity of the samples was measured in static air and in Ar, respectively, using a standard four-terminal dc method in the temperature range of 300–850 °C with a step of 50 °C. All the conductivity data were collected after equilibrium was achieved. For the thermal cycling test, the sample ($x = 0.6$) was heated to a high temperature at 5 °C min^{-1} and then cooled down naturally with a furnace to RT for the first cycle, which was followed by heating again for the second and third cycles. During the heating process in each cycle, the electrical conductivity of the sample was collected. Impedance measurement of the symmetrical cells and single-cells was performed on a Solartron 1260 impedance gain/phase analyzer in combination with a 1287 electrochemical interface in the 0.1 to 10^6 Hz frequency range with a perturbation amplitude of 10 mV in air (20 ml min^{-1}). The current–voltage (I–V) curves were recorded in the range of 700–850 °C by using a Solartron 1287 Electrochemical interface controlled by CorrWare software, where the cell voltage was varied from OCV (open circuit voltage) to 0.3 V.

3. Results and discussion

3.1. Lattice structure

Fig. 1 shows the XRD patterns of samples $La_{0.3}Sr_{0.7}Ti_{1-x}Co_xO_3$ (LSTC, $x = 0.3$–0.6), which were sintered for 10 h at 1200 °C for $x = 0.3$ and 0.45 and at 1150 °C for $x = 0.6$. All samples exhibit a single phase with a $Pm\bar{3}m$ cubic perovskite structure and no impurities can be observed in the detection limit. With increasing content of Co, the diffraction peaks of LSTC shift progressively to a high-angle direction, indicating the shrinkage of lattice parameters. This is associated with the size difference between Ti and Co ions.

In order to characterize the structure stability of LSTC during the heating process, the samples are subjected to HT-XRD examination. The typical HT-XRD results for $x = 0.6$ are shown in Fig. 2. The results reveal that the synthesized LSTC ($x = 0.3$–0.6) keep their cubic structure over the temperature range of RT–900 °C, and no structure change or phase segregation is detected, indicating the good structural stability of the synthesized LSTC samples. To obtain detailed information about the
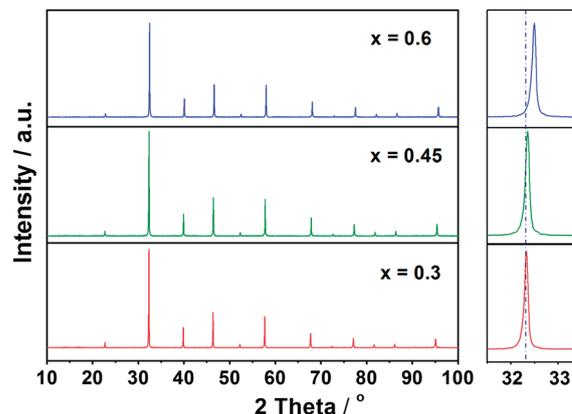

Fig. 1 XRD patterns of $La_{0.3}Sr_{0.7}Ti_{1-x}Co_xO_3$ samples sintered for 10 h at 1200 °C for $x = 0.3$ and 0.45 and at 1150 °C for $x = 0.6$.

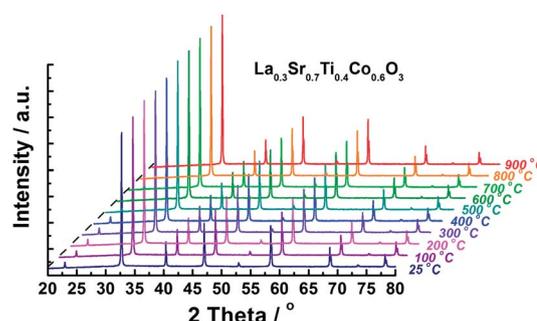**Fig. 2** XRD patterns of $La_{0.3}Sr_{0.7}Ti_{0.4}Co_{0.6}O_3$ at different temperatures.

crystal structure of the synthesized LSTC at different temperatures, Rietveld refinement is performed on the HT-XRD data using the GSAS/EXPGUI program. For all the LSTC samples, the $Pm\bar{3}m$ cubic perovskite structure is employed as an initial model, where La/Sr is located at 1a (0, 0, 0) site, Ti/Co at 1b (1/2, 1/2, 1/2) site, and O at 3c (0, 1/2, 1/2) site. The typical refinement results for samples with $x = 0.45$ at 25 and 900 °C are illustrated in Fig. 3. The refinement shows good agreement between the calculated and observed profiles. The refined structure parameters for samples at 25 and 900 °C are summarized in Table 1. The lattice parameter of samples decreases with increasing content of Co for both at 25 and 900 °C, which is consistent with the variation of the diffraction peaks in Fig. 1. This implies that the content of Co^{4+} ions increases in LSTC, taking into account the ionic radius of Co^{4+} (0.67 Å), Co^{3+} (LS: 0.685 Å, HS: 0.75 Å) and Ti^{4+} (0.745 Å),[30] and the fact that the Co^{3+} ion tends to take a higher spin state at high temperatures.[31–33]

With HT-XRD data, the lattice parameter of samples at different temperatures can be calculated by Rietveld refinement. The obtained lattice parameter variations of the investigated samples LSTC at different temperatures are depicted in Fig. 4. With the fitted linear slope, the thermal expansion coefficients of samples are derived, which are shown in the inset of Fig. 4. Two slopes with a bending at 300 °C can be observed for all three samples. The increased slope in the high
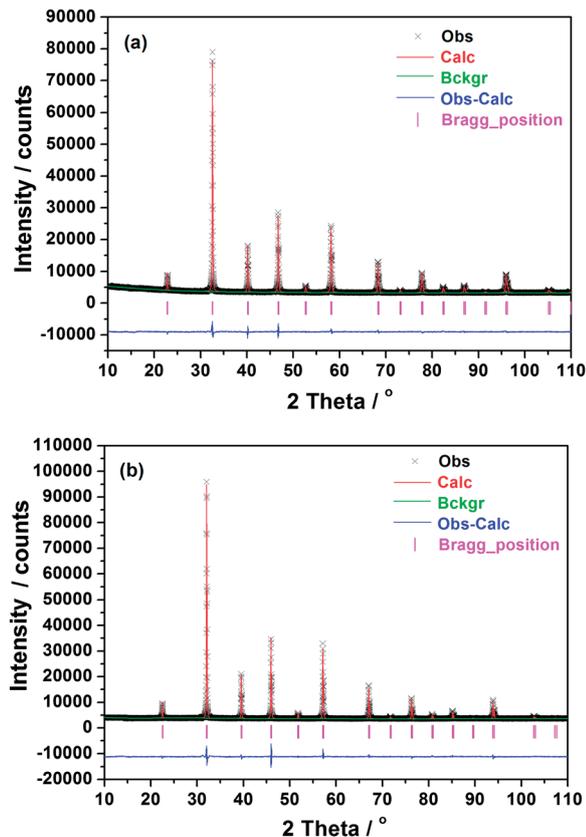
10292 | J. Mater. Chem. A, 2014, **2**, 10290–10299

This journal is © The Royal Society of Chemistry 2014

Fig. 3 XRD patterns and Rietveld refinement results of the sample with $x = 0.45$ at 25 °C (a) and 900 °C (b): observed (cross symbols) and calculated (continuous line).
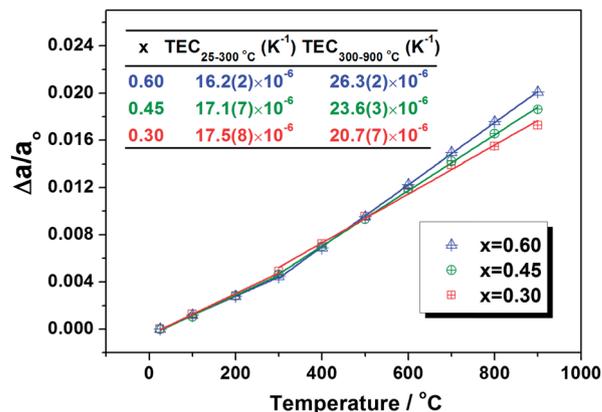

Fig. 4 Temperature dependence of the refined lattice parameter variations of different samples. The inset is the calculated thermal expansion coefficients.
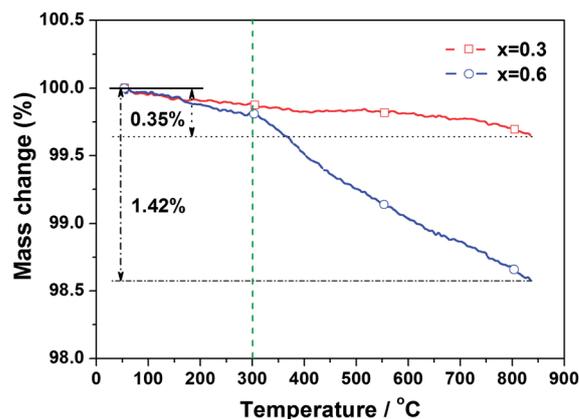

Fig. 5 TG results of LSTC ($x = 0.3$ and 0.6), indicating the weight loss (%) of samples in air.

temperature range, corresponding to a larger TEC value, is associated with the so-called chemical expansion, which is caused by the loss of lattice oxygen, reduction of B-site ions and/or transition from low-spin to high-spin state of partial Co ions.[31,34,35] In a low temperature range (RT–300 °C), all samples show almost the same slope. However, in a high temperature range, the slope increases significantly with the Co content, corresponding to the increased TEC. The TEC is 20.7(7), 23.6(3) and 26.3(2) × 10^{-6} K^{-1} for the LSTC samples with $x = 0.3$, 0.45 and 0.6, respectively. The increased TEC with increasing Co content is related to the weak Co–O bond compared to the Ti–O

bond. The high content of Co in the sample will induce more lattice oxygen loss and thus more oxygen vacancy generation and more Co ion reduction, which thus result in large lattice expansion.

This assumption is supported by TG results. As shown in Fig. 5, there is a slow weight loss in the range RT–300 °C, corresponding to a mass change of *ca.* 0.09%, which probably

Table 1 Structural parameters based on the Rietveld refinement of HT-XRD data of LSTC at 25 and 900 °C. La/Sr is located at 1a (0, 0, 0) position, Co/Ti at 1b (1/2, 1/2, 1/2), and O at 3c (0, 1/2, 1/2) sites

	$x = 0.3$		$x = 0.45$		$x = 0.60$	
	25 °C	900 °C	25 °C	900 °C	25 °C	900 °C
$a = b = c$ (Å)	3.8783(22)	3.9451(6)	3.8667(18)	3.9391(19)	3.8591(9)	3.9366(9)
La/Sr Uiso	0.0150(2)	0.0356(2)	0.0150(2)	0.0348(3)	0.0176(1)	0.0361(2)
Ti/Co Uiso	0.0077(3)	0.0206(3)	0.0074(3)	0.0182(4)	0.0105(3)	0.0281(4)
O Uiso	0.0257(6)	0.0458(7)	0.0217(6)	0.0511(17)	0.0291(7)	0.0677(9)
χ^2	2.408	3.251	2.479	2.919	4.010	4.814
R_p (%)	1.75	1.83	1.62	1.56	1.49	1.39
R_{wp} (%)	2.46	2.83	2.35	2.50	2.42	2.56

This journal is © The Royal Society of Chemistry 2014

J. Mater. Chem. A, 2014, **2**, 10290–10299 | **10293**

originated from the evaporation of absorbed water. Above 300 °C, a significant weight loss is observed for the sample with $x = 0.6$, while only a slight weight loss is detected for the sample with $x = 0.3$, demonstrating the large lattice oxygen loss of the sample with a high Co content. This is consistent with the TEC results. Although a high Co content leads to a high TEC value, it can also give rise to more oxygen vacancies, which are beneficial to the electrode reaction process. It is worth noting that the TEC derived from the lattice parameter variation upon temperature is different from that obtained by directly measuring the dense sample. Considering that the dense sample usually contains more or less pores, the calculated TEC from lattice parameter change is higher than the practically measured value.[17] Nevertheless, the calculated TEC of LSTC ($x = 0.3$–0.6) prepared in this work, 20–26 × 10^{-6} K^{-1}, is lower than the tested TEC of La$_{0.3}$Sr$_{0.7}$CoO$_{3-\delta}$ (28.8 × 10^{-6} K^{-1}), SrCo$_{0.8}$Ti$_{0.2}$O$_{3-\delta}$ (28.3 × 10^{-6} K^{-1})[36] and BSCF (24.9–27.3 × 10^{-6} K^{-1}).[35,37]

3.2. Chemical compatibility

The chemical compatibility of cathode materials with an electrolyte is an important factor affecting the long-term performance of SOFC stacks. To evaluate the chemical compatibility of LSTC with electrolyte LSGM, LSTC ($x = 0.6$) and LSGM powders are mixed in 50 : 50 weight ratio, pressed to a pellet and then sintered at 1250 °C for 5 h. The sintered pellet is crushed and ground to powders, followed by XRD examination. The XRD pattern is shown in Fig. 6. No impurity is detected in this situation, indicating a good chemical compatibility between LSTC cathode and LSGM electrolyte below 1250 °C.

3.3. Electrical conductivity

Dense pellets with relative density above 95% are employed for electrical conductivity measurement. Fig. 7 presents the electrical conductivity of samples tested under various conditions. As shown in Fig. 7(a), the conductivity of samples with $x = 0.6$ in air is higher than that in argon, showing typical p-type conduction behavior. This means that the electron–hole is the charge carrier in this material. With respect to the different samples, as displayed in Fig. 7(b), the conductivity increases
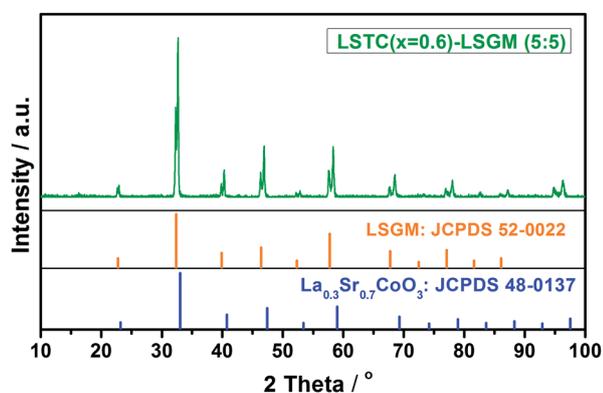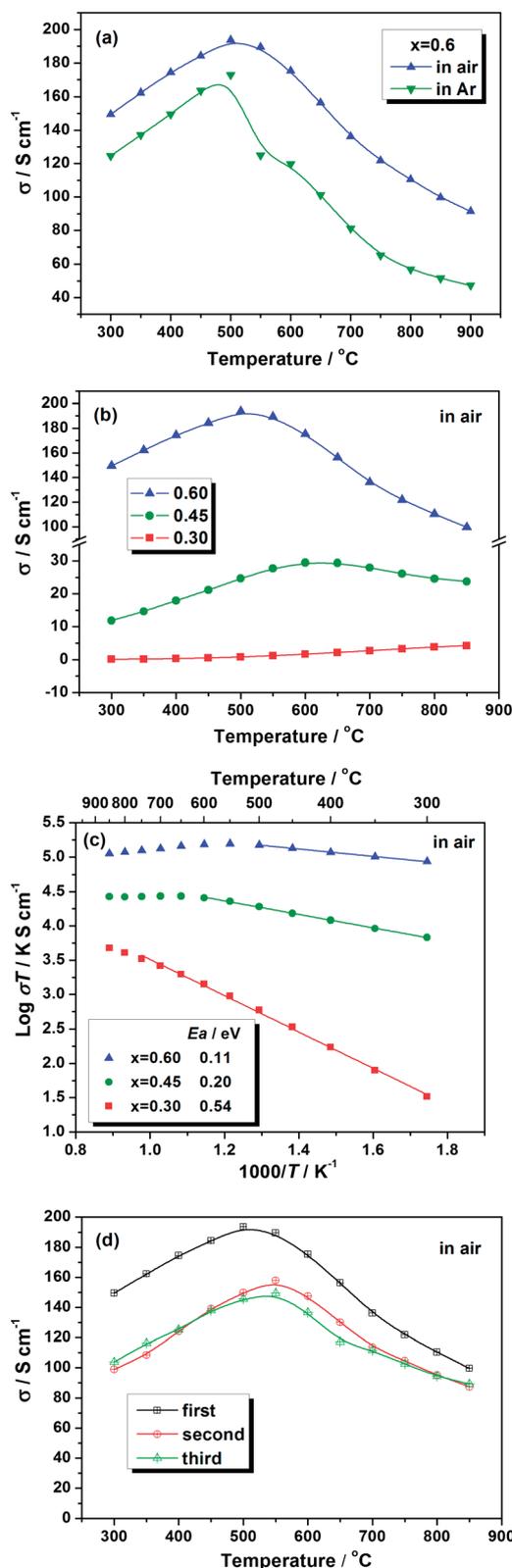

Fig. 6 XRD pattern of the LSTC–LSGM mixture calcined at 1250 °C for 5 h.

Fig. 7 (a) Temperature dependence of electrical conductivity of La$_{0.3}$Sr$_{0.7}$Ti$_{0.4}$Co$_{0.6}$O$_{3-\delta}$ in air and argon; (b) temperature dependence of electrical conductivity and (c) its Arrhenius plot of La$_{0.3}$Sr$_{0.7}$Ti$_{1-x}$Co$_x$O$_{3-\delta}$; (d) electrical conductivity of La$_{0.3}$Sr$_{0.7}$Ti$_{0.4}$Co$_{0.6}$O$_{3-\delta}$ under different thermal cycles in air.

10294 | J. Mater. Chem. A, 2014, 2, 10290–10299

This journal is © The Royal Society of Chemistry 2014

with increasing Co contents in air. For samples with $x = 0.45$ and 0.6, the conductivity shows a maximum value with temperature, it increases initially and then decreases. While, the sample with $x = 0.3$ shows very low conductivity up to 600 °C and then presents a slight increase at high temperature. In Arrhenius plot (Fig. 7(c)), all samples exhibit a linear relationship in a low temperature range, indicating small polaron conduction behavior. However, at high temperature there is a deviation from linearity, corresponding to the inflection of the conductivity curve in Fig. 7(b), which is attributed to the loss of lattice oxygen from LSTC. This process can be expressed in eqn (1) and (2). The loss of lattice oxygen leads to the simultaneous generation of oxygen vacancies and free electrons. Although the former can promote the oxygen ion transport and accelerate the electrode reaction, the latter will cause the annihilation of partial electron–holes, and thus result in the decrease of electronic conductivity. With increasing Co content, the inflection temperature of the conductivity curve decreases, which is mainly related to the weaker Co–O bond compared to the Ti–O bond.

$$O_O^\times \rightarrow 2e' + V_O^{\cdot\cdot} + \frac{1}{2}O_2 \tag{1}$$

$$e' + h^\cdot \rightarrow nil \tag{2}$$
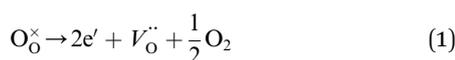
At 800 °C, the conductivity of LSTC reaches 24 and 110 S cm^{-1} for $x = 0.45$ and 0.6, respectively, which are comparable to or even higher than that of BSCF.[35]

For charge compensation of La$_{0.3}$Sr$_{0.7}$TiO$_3$ without Co-doping, it is believed that the excessive positive charge produced by La-doping at Sr-site is balanced by the formation of A-site vacancies.[25,38] With respect to the system of La$_{0.3}$Sr$_{0.7}$Ti$_{1-x}$Co$_x$O$_3$, when $x = 0.3$, the excessive positive charge of La can be balanced by the substitution of Co for Ti, as expressed in eqn (3), provided that the oxygen vacancy concentration is limited in air. Because both Co^{3+} and Ti^{4+} ions are in the stable oxidation state and no electron defect is generated, the sample La$_{0.3}$Sr$_{0.7}$Ti$_{0.7}$Co$_{0.3}$O$_3$ shows a much lower conductivity.

$$0.3\left[La_{sr}^{\cdot}\right] = 0.3\left[Co_{Ti^{4+}}^{3+\prime}\right] \tag{3}$$
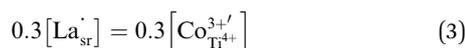
For further substitution of Co for Ti ($x = 0.45$ and 0.6), the extra Co ions will take the oxidation state of Co^{4+} in order to keep the neutrality of the material. Considering that considerable oxygen vacancies may produce in Co-rich samples, which will cause the generation of free electrons as shown in eqn (1), the solid solution formula of La$_{0.3}$Sr$_{0.7}$Ti$_{1-x}$Co$_x$O$_{3-\delta}$ can be written as:

$$La_{0.3}^{3+}Sr_{0.7}^{2+}Ti_{1-x}^{4+}Co_{0.3+2\delta}^{3+}Co_{x-0.3-2\delta}^{4+}O_{3-\delta}$$
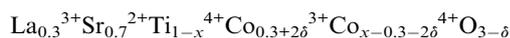
Accordingly, the concentration [Co^{4+}], corresponding to the concentration of electron–holes [h$^\cdot$], is proportional to the Co content x. As a result, the electronic conductivity increases with the Co content in LSTC materials, which is consistent with the results shown in Fig. 7(b).

To confirm the assumption discussed above, XPS examination is performed to identify the oxidation state of Co ions in LSTC. The evolution of the Co 2p photoelectron spectra as a function of doping amount is shown in Fig. 8. Two broad peaks, belonging to Co 2p$_{3/2}$ and Co 2p$_{1/2}$ electrons, were observed, both of which can be deconvoluted into two peaks, assignable to Co^{3+} and Co^{4+}, respectively.[39–41] With the integrated area of the peaks, the contents of each oxidation state of Co ions are calculated, which are listed in Fig. 8. Besides Co^{3+}, a considerable amount of Co^{4+} is detected in both samples and the content of Co^{4+} increases with increasing Co doping level, from 24% ($x = 0.45$) to 48% ($x = 0.6$). This result is consistent with the assumption of charge compensation. A satellite peak at around 786 eV was evident, suggesting a small amount of Co^{2+} coexisting on the surface of LSTC particles.[40,42]

In order to evaluate the performance stability of LSTC during the thermal cycling process, the conductivity of the sample with high Co content ($x = 0.6$) is tested under different cycles. The result is shown in Fig. 7(d). The sample shows similar conductivity during the second and third cycles but much lower than that in the first cycle. The conductivity of mixed conductors depends strongly on the thermal history they experienced. As mentioned above, some lattice oxygen may lose at high temperature in the sintering process, which can lead to the
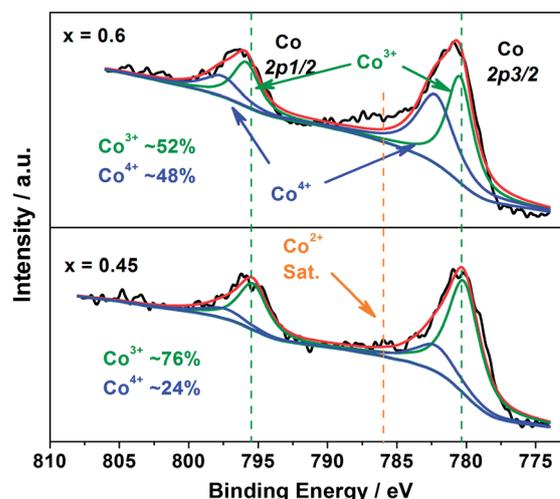

Fig. 8 XPS spectra of Co 2p of the synthesized La$_{0.3}$Sr$_{0.7}$Ti$_{1-x}$Co$_x$O$_3$ ($x = 0.45$ and 0.6).
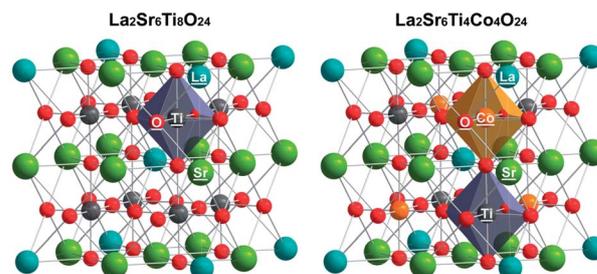
Fig. 9 Structure models of La$_2$Sr$_6$Ti$_8$O$_{24}$ and La$_2$Sr$_6$Ti$_4$Co$_4$O$_{24}$ for first-principles calculation.
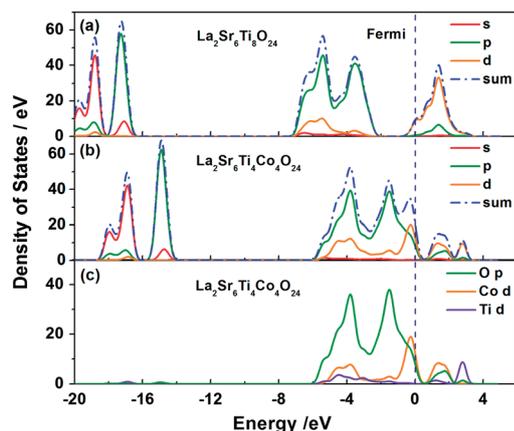
Fig. 10 Density of states of (a) $La_2Sr_6Ti_8O_{24}$ and (b) $La_2Sr_6Ti_4Co_4O_{24}$; (c) detailed view of the states of O p, Co d and Ti d. Dashed lines represent the Fermi energy.

decrease in conductivity. During the cooling process, these oxygen vacancies can be incorporated into the bulk of the sample again in order to maintain the thermodynamic
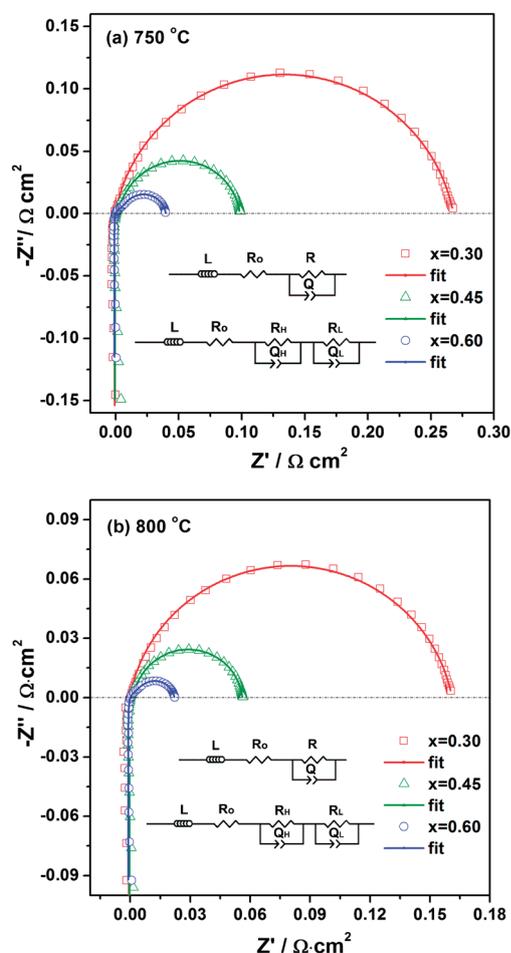
equilibrium. In the case of fast cooling, however, this process cannot be thoroughly completed due to kinetic reasons, and more oxygen vacancies will remain, leading to reduced electrical conductivity. Because the thermal insulation system of the furnace for sample preparation in our lab is much better than that for electrical conductivity measurement, the sample, which has ever experienced the conductivity test and thus been subjected to the fast cooling process, usually presents a much lower conductivity value than the initial one. Fortunately, the sample displays similar electrical conductivity values in the subsequent cycles, demonstrating the highly reversibility of the structure and the good thermal cycling performance of LSTC as the cathode for SOFCs.

To get insight into the effect of Co-doping on the electronic conductivity of the LSTC, first-principles calculations are performed to get the density of states (DOS) based on density functional theory using Materials Studio software. For simplicity, $La_2Sr_6Ti_8O_{24}$ and $La_2Sr_6Ti_4Co_4O_{24}$ are approximately used as the calculation models for $La_{0.3}Sr_{0.7}TiO_3$ with and without Co-doping (Fig. 9). The calculated results are shown in Fig. 10. Significantly, Co-doping changes the density of states of electrons in LSTC. LSTC has transformed from n-type conductor (LST) to p-type conductor, since the Fermi level shifts from the conduction band (Fig. 10(a)) to the valence band (Fig. 10(b)). This finding is in good agreement with the experimental results (Fig. 7) and the previous reports that LST exhibits n-type conduction behavior under reducing atmosphere while Sr-doped $LaCoO_3$ shows p-type conduction characteristics.[43–45] The remarkably high conductivity values of LSTC ($x = 0.45$ and 0.6) are mainly attributed to the narrow bandgap and the observed strong hybridization of the Co and O states at the valence band edge and conduction band (Fig. 10(b) and (c)). Both of them

Fig. 11 Impedance spectra results of symmetrical cells LSTC|LSGM|LSTC measured in air at 750 °C (a) and 800 °C (b). The ohmic resistance has been subtracted from the impedance for direct comparison. Insets are the equivalent circuits adopted for data fitting.

Table 2 Polarization resistances as a function of temperature for the symmetrical cell LSTC|LSGM|LSTC in air under the zero dc condition obtained from the data fitting with equivalent circuit $LR_O(Q_HR_H)(Q_LR_L)$ and $LR_O(QR)$

T/°C		700	750	800	850
0.3	R/Ω cm^2	0.498	0.268	0.162	0.104
	C/F cm^{-2}	0.073	0.061	0.055	0.052
	F/Hz	4.38	9.76	18.01	29.36
	ASR/Ω cm^2	0.498	0.268	0.162	0.104
0.45	R_H/Ω cm^2	0.0195	0.0090	0.0045	0.0023
	C_H/F cm^{-2}	0.167	0.160	0.111	0.116
	F_H/Hz	48.91	109.97	317.34	612.19
	R_L/Ω cm^2	0.220	0.091	0.053	0.035
	C_L/F cm^{-2}	0.202	0.211	0.191	0.168
	F_L/Hz	3.57	8.27	15.73	26.84
	ASR/Ω cm^2	0.2395	0.1000	0.0575	0.0373
0.6	R_H/Ω cm^2	0.0150	0.0079	0.0043	0.0025
	C_H/F cm^{-2}	0.102	0.086	0.085	0.101
	F_H/Hz	102.44	236.01	430.75	637.36
	R_L/Ω cm^2	0.078	0.033	0.019	0.012
	C_L/F cm^{-2}	0.575	0.475	0.393	0.339
	F_L/Hz	3.56	10.08	21.30	37.66
	ASR/Ω cm^2	0.0930	0.0409	0.0233	0.0145

lead to low activation energy for electron–holes jumping along the Co–O–Co bonding network.

3.4. Electrochemical performance

The cathode performance of LSTC is evaluated by symmetrical cells LSTC|LSGM|LSTC with AC impedance in the temperature range of 700–850 °C. The typical Nyquist plots and fitting results with equivalent circuit $LR_O(Q_HR_H)(Q_LR_L)$ are shown in Fig. 11, where L is the inductance, R_O stands for the ohmic resistance, and (Q_HR_H) and (Q_LR_L) represent the constant phase element and resistance of the processes at high and low frequencies, respectively. Because only one arc is observed for the sample with $x = 0.3$, $LR_O(QR)$ is used for data fitting. The area specific resistances (ASRs) of the LSTC electrode, the characteristic capacitances and frequencies $(C = (QR)^{1/n}/R, f = 1/2\pi(QR)^{1/n})$ of the arcs are summarized in Table 2.
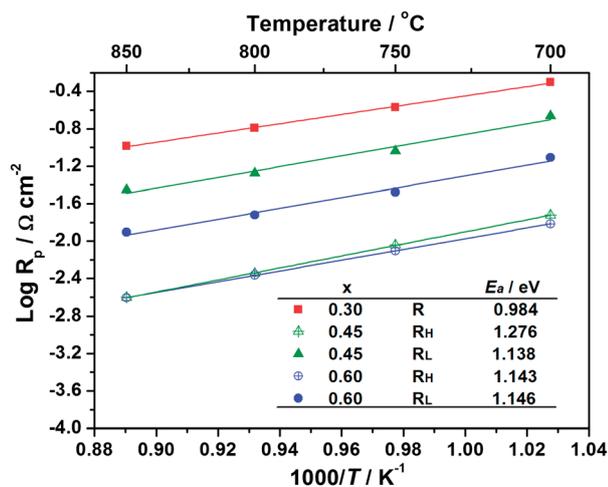
It is suggested that the high frequency arc is mainly related to the charge transfer process, while the low frequency arc is associated with the molecular oxygen dissociation process,[46–49] as expressed in eqn (4) and (5). Since the low frequency arc is much larger than the high frequency arc, the rate-limiting step of the electrode reaction should be the molecular oxygen dissociation processes.

$$O_{ad} + e' \leftrightarrow O'_{ad} \quad (4)$$

$$O_{2,ad} \leftrightarrow 2O_{ad} \quad (5)$$

The various resistances *versus* reciprocal temperature, accompanying with activation energy, are shown in Fig. 12. All the resistances (R_H and R_L) decrease noticeably with increasing

Fig. 12 Polarization resistances *versus* reciprocal temperature for the $La_{0.3}Sr_{0.7}Ti_{1-x}Co_xO_{3-\delta}$ cathode obtained in air.

Table 3 ASR of the typical reported cathode materials based on the LSGM electrolyte and the prepared $La_{0.3}Sr_{0.7}Ti_{0.4}Co_{0.6}O_{3-\delta}$ in this work

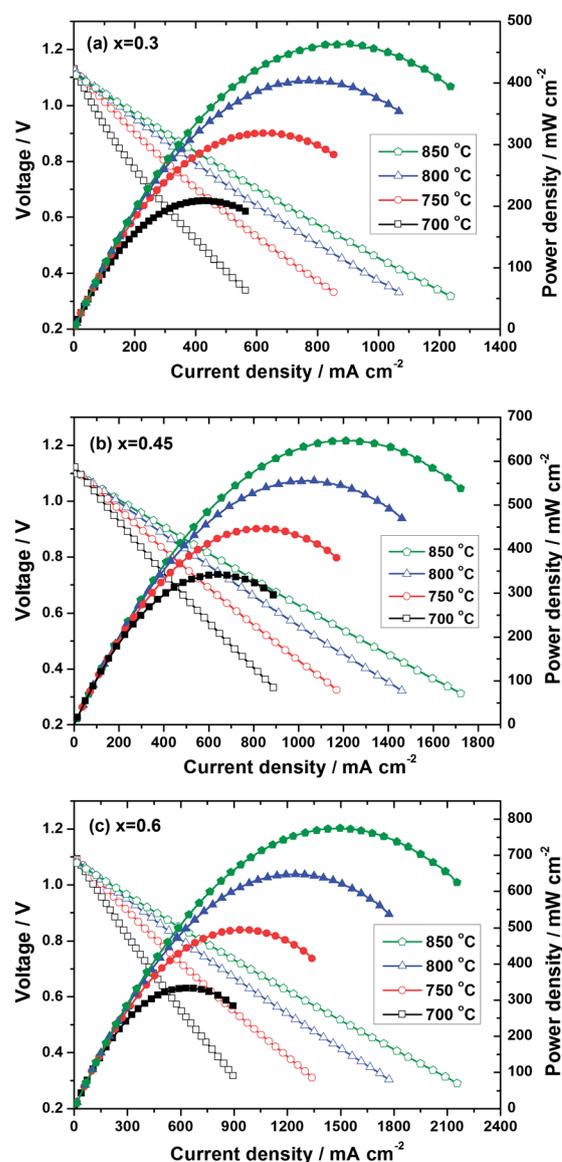| Composition	Temperature/°C	ASR/Ω cm²	Reference
$SmBaCo_2O_{5+x}$	800	0.031	50
$PrBa_{0.5}Sr_{0.5}Co_2O_{5+x}$	800	0.027	51
$GdBaCo_2O_{5+\delta}$	800	~0.138	52
$Ba_{0.5}Sr_{0.5}Co_{0.8}Fe_{0.2}O_{3-\delta}$	800	~0.075	52
$Sr_{0.7}Y_{0.3}CoO_{2.65-\delta}$	800	0.11	53
$Sm_{0.5}Sr_{0.5}CoO_{3-\delta}$	800	1.34	54
$La_{0.6}Sr_{0.4}Fe_{0.8}Co_{0.2}O_{3-\delta}$	700	0.1	55
$Pr_2NiO_{4+\delta}$	700	0.23	55
$La_{1.7}Ca_{0.3}Ni_{0.7}Cu_{0.3}O_{4+\delta}$	800	0.099	56
$SrCo_{0.9}Nb_{0.1}O_{3-\delta}$	800	0.029	57
$BaCo_{0.7}Fe_{0.2}Nb_{0.1}O_{3-\delta}$	750	0.06	58
$Ba_{0.9}Co_{0.7}Fe_{0.2}Nb_{0.1}O_{3-\delta}$	800	0.02	59
	700	0.0930	This work
$La_{0.3}Sr_{0.7}Ti_{0.4}Co_{0.6}O_{3-\delta}$	750	0.0409	This work
	800	0.0233	This work

Fig. 13 Voltage and power density *versus* current density plots for single-cell LSTC/LSGM/LDC/(Ni–GDC) with humidified pure hydrogen as fuel and pure oxygen as an oxidant, (a) $x = 0.3$; (b) $x = 0.45$ and (c) $x = 0.6$.

This journal is © The Royal Society of Chemistry 2014

J. Mater. Chem. A, 2014, **2**, 10290–10299 | **10297**

temperature, indicative of thermal activation behavior of the electrode reaction process. With increasing Co content, all the R_H and R_L decrease significantly, demonstrating that Co-doping improves the molecular oxygen dissociation and charge transfer processes of the electrode. The sample with $x = 0.6$ yields the lowest area-specific resistance of 0.0145 Ω cm^2 at 850 °C, followed by $x = 0.45$ and 0.3 with ASR of 0.0373 and 0.104 Ω cm^2, respectively, indicating that the electrode performance is significantly enhanced by Co substitution. The ASR of the LSTC electrode with $x = 0.6$ is superior to and comparable with the reported typical cathode materials based on the LSGM electrolyte, as summarized in Table 3.

In order to evaluate the cathodic properties of LSTC, the LSGM electrolyte-supported single cell with the configuration of LSTC/LSGM/LDC/(Ni–GDC) is constructed and the performance is examined (Fig. 13). The open circuit voltage (OCV) of the cells is about 1.10 V at 850 °C, which is very close to the theoretical

value ($\sim$1.13 V), indicating that the gas leakage is very small. The cell performance of LSTC is remarkably enhanced by Co substitution. At 850 °C, the maximum power density with O$_2$ as an oxidant is 464.5, 648 and 775 mW cm^{-2} for $x = 0.3$, 0.45 and 0.6, respectively, revealing the LSTC as a quite potential cathode material. With air as an oxidant, the cell with LSTC ($x = 0.45$) delivers the maximum power density of 597 mW cm^{-2} at 850 °C (Fig. 14), just slightly lower than that in pure O$_2$. Considering that the thickness of the LSGM electrolyte used in the single-cell is about 400 μm, the cell performance is acceptable, which can be further enhanced by using a thinner LSGM electrolyte and optimizing the electrode structure. The cell microstructure after the test is provided in Fig. 15. The electrodes still maintain the porous structure and good connection with the LSGM electrolyte. The excellent performance of electrolyte-supported single cells with the LSTC cathode is a strong indication of its potential as a cathode material for SOFCs.

4. Conclusions

The perovskites La$_{0.3}$Sr$_{0.7}$Ti$_{1-x}$Co$_x$O$_3$ ($x = 0.3$, 0.45 and 0.6) are prepared and investigated as potential cathode materials for IT-SOFCs. All the LSTC compounds show a cubic structure with lattice parameter decreasing upon Co substitution. The TECs of LSTC, derived from HT-XRD data, increase with the Co content. The LSTC samples with $x = 0.3–0.6$ exhibit the TEC of 20.7–26.3 $\times$ 10^{-6} K^{-1} in the temperature range of 300–900 °C. Co substitution enhances significantly the electrical conductivity of LSTC due to the increased concentration of electronic holes and the reduced bandgap energy. LSTC has good chemical compatibility with the LSGM electrolyte below 1250 °C. The Co substitution promotes the molecular oxygen dissociation and electron charge transfer processes occurring on the electrode–gas interface, sequentially decreases the ASR of the LSTC electrode and increases the power density of single-cells. The maximum power density of the LSGM electrolyte-supported single-cell with LSTC as the cathode increases with the Co content and can reach the value of 464.5, 648, and 775 mW cm^{-2} at 850 °C in pure O$_2$ for $x = 0.3$, 0.45, and 0.6, respectively. With air as an oxidant, the maximum power density is 597 mW cm^{-2} for $x = 0.45$. The high performance makes the LSTC ($x = 0.45$ and 0.6) promising candidates as cathode materials for IT-SOFCs.

Fig. 14 Voltage and power density *versus* current density plots for single-cell LSTC ($x = 0.45$)/LSGM/LDC/(Ni–GDC) with humidified pure hydrogen as fuel and air as an oxidant.

Acknowledgements

Notes and references

1 S. C. Singhal, *Solid State Ionics*, 2000, **135**, 305–313.
2 S. C. Singhal, *Solid State Ionics*, 2002, **152–153**, 405–410.
3 S. McIntosh and R. J. Gorte, *Chem. Rev.*, 2004, **104**, 4845–4865.
4 B. C. H. Steele, *Nature*, 1999, **400**, 619.

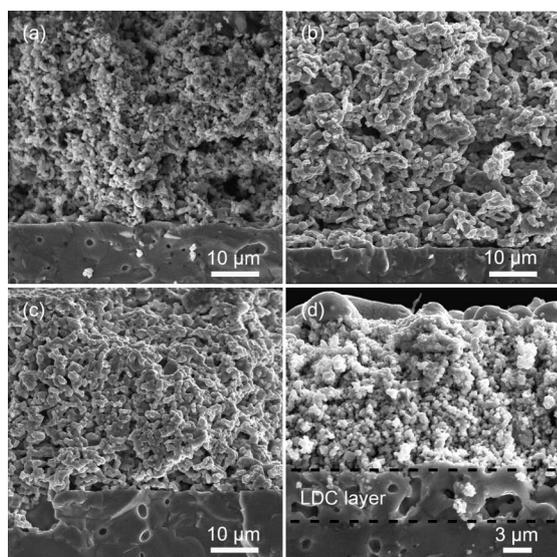**Fig. 15** SEM micrographs of the cross-section of the tested cells: LSTC cathode on LSGM electrolyte with (a) $x = 0.3$, (b) $x = 0.45$, (c) $x = 0.6$; (d) Ni–GDC anode with an LDC buffer layer.

10298 | *J. Mater. Chem. A*, 2014, **2**, 10290–10299

This journal is © The Royal Society of Chemistry 2014

5 E. D. Wachsman and K. T. Lee, *Science*, 2011, **334**, 935–939.

6 B. C. H. Steele and A. Heinzel, *Nature*, 2001, **414**, 345–352.

7 Z. Tianshu, P. Hing, H. Huang and J. Kilner, *Solid State Ionics*, 2002, **148**, 567–573.

8 T. Ishihara, H. Matsuda and Y. Takita, *J. Am. Chem. Soc.*, 1994, **116**, 3801–3803.

9 M. S. D. Read, M. S. Islam, G. W. Watson, F. King and F. E. Hancock, *J. Mater. Chem.*, 2000, **10**, 2298–2305.

10 K. Huang, M. Feng, J. B. Goodenough and M. Schmerling, *J. Electrochem. Soc.*, 1996, **143**(11), 3630–3636.

11 S. Khan, R. J. Oldman, F. Corà, C. R. A. Catlow, S. A. French and S. A. Axon, *Phys. Chem. Chem. Phys.*, 2006, **8**, 5207–5222.

12 Y. Shen, H. Zhao, K. Świerczek, Z. Du and Z. Xie, *J. Power Sources*, 2013, **240**, 759–765.

13 A. Tarancón, M. Burriel, J. Santiso, S. J. Skinner and J. A. Kilner, *J. Mater. Chem.*, 2010, **20**, 3799–3813.

14 C. Sun, R. Hui and J. Roller, *J. Solid State Electrochem.*, 2010, **14**, 1125–1144.

15 Z. Shao and S. M. Haile, *Nature*, 2004, **431**, 170–173.

16 A. Bieberle-Hütter, M. Søgaard and H. L. Tuller, *Solid State Ionics*, 2006, **177**(19), 1969–1975.

17 C. Kuroda, K. Zheng and K. Świerczek, *Int. J. Hydrogen Energy*, 2013, **38**, 1027–1038.

18 H. Zhao, D. Teng, X. Zhang, C. Zhang and X. Li, *J. Power Sources*, 2009, **186**, 305–310.

19 R. Martínez-Coronado, A. Aguadero, D. Pérez-Coll, L. Troncoso, J. A. Alonso and M. T. Fernández-Díaz, *Int. J. Hydrogen Energy*, 2012, **37**, 18310–18318.

20 X. Li, H. Zhao, X. Zhou, N. Xu, Z. Xie and N. Chen, *Int. J. Hydrogen Energy*, 2010, **35**, 7913–7918.

21 O. A. Marina, N. L. Canfield and J. W. Stevenson, *Solid State Ionics*, 2002, **149**, 21–28.

22 P. I. Cowin, C. T. G. Petit, R. Lan, J. T. S. Irvine and S. Tao, *Adv. Energy Mater.*, 2011, **1**, 314–332.

23 X. Li, H. Zhao, F. Gao, N. Chen and N. Xu, *Electrochem. Commun.*, 2008, **10**, 1567–1570.

24 X. Li, H. Zhao, N. Xu, X. Zhou, C. Zhang and N. Chen, *Int. J. Hydrogen Energy*, 2009, **34**, 6407–6414.

25 F. Napolitano, D. G. Lamas, A. Soldati and A. Serquis, *Int. J. Hydrogen Energy*, 2012, **37**, 18302–18309.

26 M. Yuste, J. C. Pérez-Flores, J. R. Paz, M. T. Azcondo, F. García-Alvarado and U. Amador, *Dalton Trans.*, 2011, **40**, 7908–7915.

27 A. C. Larson and R. B. Von Dreele, *Los Alamos Natl. Lab., [Rep.] LA*, 1994, 86–748, LAUR.

28 B. H. Toby, *J. Appl. Crystallogr.*, 2001, **34**, 210–213.

29 J. Wang, H. Zhao, Y. Shen, Z. Du, X. Chen and Q. Xia, *ChemPlusChem*, 2013, **78**(12), 1530–1535.

30 R. D. Shannon, *Acta Crystallogr., Sect. A: Cryst. Phys., Diffr., Theor. Gen. Crystallogr.*, 1976, **32**, 751.

31 K. Huang, H. Y. Lee and J. B. Goodenough, *J. Electrochem. Soc.*, 1998, **145**, 3220.

32 M. A. Korotin, S. Y. Ezhov, I. V. Solovyev, V. I. Anisimov, D. I. Khomskii and G. A. Sawatzky, *Phys. Rev. B: Condens. Matter Mater. Phys.*, 1996, **54**(8), 5309.

33 A. Podlesnyak, S. Streule, J. Mesot, M. Medarde, E. Pomjakushina, K. Conder, A. Tanaka, M. W. Haverkort and D. I. Khomskii, *Phys. Rev. Lett.*, 2006, **97**(24), 247208.

34 Z. Shao, W. Yang, Y. Cong, H. Dong, J. Tong and G. Xiong, *J. Membr. Sci.*, 2000, **172**, 177–188.

35 B. Wei, Z. Lü, S. Li, Y. Liu, K. Liu and W. Su, *Electrochem. Solid-State Lett.*, 2005, **8**(8), A428–A431.

36 V. V. Kharton, A. A. Yaremchenko, A. V. Kovalevsky, A. P. Viskup, E. N. Naumovich and P. F. Kerko, *J. Membr. Sci.*, 1999, **163**(2), 307–317.

37 P. Ried, P. Holtappels, A. Wichser, A. Ulrich and T. Graule, *J. Electrochem. Soc.*, 2008, **155**(10), B1029–B1035.

38 S. Hashimoto, L. Kindermann, F. W. Poulsen and M. Mogensen, *J. Alloys Compd.*, 2005, **397**, 245–249.

39 E. Y. Konysheva, S. M. Francis, J. T. S. Irvine, A. Rolle and R. N. Vannier, *J. Mater. Chem.*, 2011, **21**, 15511–15520.

40 Z. Cai, M. Kubicek, J. Fleig and B. Yildiz, *Chem. Mater.*, 2012, **24**, 1116–1127.

41 E. Konysheva, R. Blackley and J. T. S. Irvine, *Chem. Mater.*, 2010, **22**, 4700–4711.

42 Z. Cai, Y. Kuru, J. W. Han, Y. Chen and B. Yildiz, *J. Am. Chem. Soc.*, 2011, **133**, 17696–17704.

43 P. R. Slater, D. P. Fagg and J. T. S. Irvine, *J. Mater. Chem.*, 1997, **7**(12), 2495–2498.

44 C. D. Savaniu and J. T. S. Irvine, *J. Mater. Chem.*, 2009, **19**, 8119–8128.

45 J. Mizusaki, J. Tabuchi, T. Matsuura, S. Yamauchi and K. Fueki, *J. Electrochem. Soc.*, 1989, **136**(7), 2082–2088.

46 M. J. Escudero, A. Aguadero, J. A. Alonso and L. Daza, *J. Electroanal.Chem.*, 2007, **611**, 107–116.

47 D. Chen, R. Ran, K. Zhang, J. Wang and Z. Shao, *J. Power Sources*, 2009, **188**, 96–105.

48 F. Mauvy, C. Lalanne, J. M. Bassat, J. C. Grenier, H. Zhao, L. Huo and P. Stevens, *J. Electrochem. Soc.*, 2006, **153**(8), A1547–A1553.

49 J. Penã-Martínez, D. Marrero-López, J. C. Ruiz-Morales, P. Núñez, C. Sánchez-Bautista, A. J. Dos Santos-García and J. Canales-Vázquez, *Int. J. Hydrogen Energy*, 2009, **34**, 9486–9495.

50 Q. Zhou, T. He and Y. Ji, *J. Power Sources*, 2008, **185**, 754–758.

51 S. Lü, G. Long, X. Meng, Y. Ji, B. Lü and H. Zhao, *Int. J. Hydrogen Energy*, 2012, **37**, 5914–5919.

52 J. Peña-Martínez, A. Tarancón, D. Marrero-López, J. C. Ruiz-Morales and P. Núñez, *Fuel Cells*, 2008, **08**(5), 351–359.

53 Y. Li, Y. N. Kim, J. Cheng, J. A. Alonso, Z. Hu, Y. Y. Chin, T. Takami, M. T. Fernández-Díaz, H. J. Lin, C. T. Chen, L. H. Tjeng, A. Manthiram and J. B. Goodenough, *Chem. Mater.*, 2011, **23**, 5037–5044.

54 T. Duong and D. R. Mumm, *J. Power Sources*, 2013, **241**, 281–287.

55 B. Philippeau, F. Mauvy, C. Mazataud, S. Fourcade and J. C. Grenier, *Solid State Ionics*, 2013, **249–250**, 17–25.

56 Y. Shen, H. Zhao, K. Świerczek, Z. Du and Z. Xie, *J. Power Sources*, 2013, **240**, 759–765.

57 F. Wang, Q. Zhou, T. He, G. Li and H. Ding, *J. Power Sources*, 2010, **195**, 3772–3778.

58 Z. Yang, C. Yang, B. Xiong, M. Han and F. Chen, *J. Power Sources*, 2011, **196**, 9164–9168.

59 Z. Yang, C. Yang, C. Jin, M. Han and F. Chen, *Electrochem. Commun.*, 2011, **13**, 882–885.

This journal is © The Royal Society of Chemistry 2014

J. Mater. Chem. A, 2014, **2**, 10290–10299 | **10299**